Carbon Defect Characterization of Nitrogen-Doped Reduced Graphene Oxide Electrocatalysts for the Two-Electron Oxygen Reduction Reaction

Hyo Won Kim,[†,‡] Hun Park,[∥] Ji Soo Roh,[⊥] Jae Eun Shin,[⊥] Tae Hoon Lee,[⊥] Liang Zhang,[§] Young Hoon Cho,[#] Hee Wook Yoon,[&] Vanessa J. Bukas,[%,@] Jinghua Guo,[§,$] Ho Bum Park,[⊥] Tae Hee Han,[∥] and Bryan D. McCloskey*[,†,‡]

[†]Department of Chemical and Biomolecular Engineering, University of California, Berkeley, Berkeley, California 94720, United States

[‡]Energy Storage and Distributed Resources Division and [§]Advanced Light Source, Lawrence Berkeley National Laboratory, Berkeley, California 94720, United States

[∥]Department of Organic and Nano Engineering and [⊥]Department of Energy Engineering, Hanyang University, Seoul 04763, Korea

[#]Membrane Research Center, Korea Research Institute of Chemical Technology, Daejeon 34114, Korea

[&]Department of Chemical Engineering, Texas Materials Institute, Center for Energy and Environmental Resources, University of Texas at Austin, Austin, Texas 78758, United States

[%]SUNCAT Center for Interface Science and Catalysis, Department of Chemical Engineering, Stanford University, Stanford, California 94305-5025, United States

[@]SUNCAT Center for Interface Science and Catalysis, SLAC National Accelerator Laboratory, 2575 Sand Hill Road, Menlo Park, California 94025, United States

[$]Department of Chemistry and Biochemistry, University of California, Santa Cruz, Santa Cruz, California 95064, United States

ABSTRACT: Numerous modified-carbon catalysts have been developed for the direct synthesis of hydrogen peroxide through electrochemical oxygen reduction. However, given the complex structure of most porous carbons and the poor oxygen reduction reaction (ORR) selectivity typically observed when they are used as catalysts, it is still unclear which carbon defects are responsible for the high two-electron ORR activity typically observed in these materials. Here, we study electrocatalytic peroxide formation activity of nitrogen-doped reduced graphene oxide (*N*-rGO) materials to relate carbon defects to electrocatalytic activity. To do so, we selected two *N*-rGO electrodes that selectively produce peroxide at all potentials studied (0.70−0.10 V vs RHE) under alkaline conditions. Oxygen reduction studies, combined with material characterization, especially solid-state ^{13}carbon nuclear magnetic resonance coupled with magic angle spinning and cross-polarization, demonstrate that epoxy or ether groups in the *N*-rGO catalyst are likely associated with the active sites that form peroxide at the lowest overpotential in alkaline media.

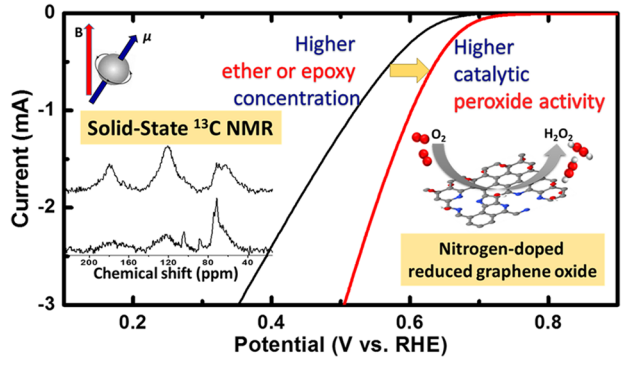

The electrochemical oxygen reduction reaction (ORR) is important for the development of many sustainable energy technologies.[1−6] In general, the ORR can proceed through one of two overall reactions in alkaline conditions:[3−5,7]

$$O_2 + 2H_2O + 4e^- \rightarrow 4OH^- \quad U^\circ = 1.23 \text{ V vs RHE} \qquad (1)$$

$$O_2 + H_2O + 2e^- \rightarrow HO_2^- + OH^- \quad U^\circ = 0.76 \text{ V vs RHE} \qquad (2)$$

U° is the standard equilibrium potential for each reaction, calculated from the free energy of each reaction, and RHE is the reversible hydrogen electrode.[8] Both 4e$^-$ and 2e$^-$ reactions are important because reaction 1 serves as the desirable cathode reaction for alkaline fuel cells, whereas reaction 2 produces hydrogen peroxide, the environmentally friendly commodity oxidant for many large-scale industrial processes, in its deprotonated form.[4,9,10] Electrodes composed of precious metals, such as platinum (for 4e$^-$ ORR) or gold−platinum−nickel nanoparticles (for 2e$^-$ ORR), generally have the best

known catalytic oxygen reduction properties in terms of activity and selectivity.[3,5,11−14] In alkaline conditions, some carbon electrodes have achieved catalytic efficiency comparable to these noble metal catalysts for both reactions 1 and 2.[4,15−19] Thus, numerous recent studies have identified various modified carbons as promising alternatives to expensive metal catalysts under alkaline conditions, particularly for the 2e$^-$ ORR (reaction 2).[15−21] These studies build upon decades of research that explored ORR on well-defined carbon-based materials, such as glassy carbon and oriented pyrolytic graphite, that were shown to be selective for hydrogen peroxide generation.[22−26]

However, the discovery that nitrogen-doped carbons, including nitrogen-doped reduced graphene oxide (*N*-rGO), can selectively catalyze the 4e$^-$ ORR (reaction 1) in alkaline conditions has triggered intense research into their activity, selectivity, and stability.[15,21,27] Unfortunately, poorly designed nitrogen-doped carbon catalysts can activate both 2e$^-$ and 4e$^-$ ORR, thereby resulting in mixed selectivity that is undesired for fuel cells that rely on reaction 1.[18,20] To address mixed ORR selectivity, researchers have attempted to identify the active sites for the 4e$^-$ oxygen reduction pathway in a variety of nitrogen-doped carbons.[7,21,28,29] On the other hand, less effort has been placed on understanding what active sites selectively promote the 2e$^-$ ORR. Identifying such sites would be beneficial for future carbon-based catalyst designs so that these sites could be eliminated from catalysts where 4e$^-$ ORR is required or to increase their concentration to enable more efficient 2e$^-$ ORR.

Studies using porous carbon catalysts have primarily presented two opposing views on 2e$^-$ active sites. One view is that 2e$^-$ ORR is promoted by sites related to sp^3 carbons at edge sites or that result from basal plane vacancies, while others have suggested sp^2-type defects close to heteroatom sites.[30,31] As a large subsection of the latter view, certain oxygen functional groups, such as catechol and hydroquinone/quinone couples, have also been proposed to facilitate peroxide formation under alkaline conditions.[23,26] Carbon electrodes with other heteroatoms, including nitrogen and fluorine, have been investigated as a means of improving 2e$^-$ ORR catalytic activity and stability.[32,33] It has been proposed that heteroatoms with a higher electronegativity activate π electrons and induce charge redistribution, which changes ORR intermediate adsorption on carbon materials to favor peroxide generation.[32,33] However, it is still a challenge to accurately correlate specific oxygen functionality with efficient peroxide formation.[23,26,30−33]

A recent study of well-defined nitrogen-doped nanocarbons has suggested the possibility that carbon atoms near electron-withdrawing pyridinic nitrogen are related to ORR activity regardless of 2e$^-$/4e$^-$ selectivity.[34] More recently, oxidized nanocarbons, including nanotubes and mildly reduced GO, without nitrogen doping have been shown to significantly improve peroxide formation activity in alkaline media due to the high activity of defect sites related to ether or carboxylic acid groups.[16,17] Of note, it is widely accepted that more defective carbon materials exhibit higher catalytic activity for the 2e$^-$ ORR.[35,36] However, detailed studies on carbon defects for the 2e$^-$ reaction are still lacking given the difficulty of identifying carbon catalyst active sites.

Here, we attempt to relate electrocatalytic peroxide formation activity to carbon defects associated with oxygen- and nitrogen-containing groups within *N*-rGO materials in alkaline conditions. To do so, we first synthesized two *N*-rGO materials with different defect compositions, both of which catalyze 2e$^-$ ORR selectively at pH 13, albeit with different activities. The carbon defects in each of the synthesized *N*-rGO materials were characterized by solid-state carbon-13 nuclear magnetic resonance (^{13}C ssNMR) with magic angle spinning (MAS) and common X-ray-based tools, including X-ray photoelectron spectroscopy (XPS) and near-edge X-ray absorption fine structure (NEXAFS). Our results reveal that high 2e$^-$ alkaline ORR activity is related to the inclusion of epoxy and ether groups in the *N*-rGO structure rather than other functional groups, including those related to nitrogen.

Generally, typical nitrogen doping of GO has been conducted through one of two main procedures: hydrothermal treatment or pyrolysis in the presence of a small molecule nitrogen-doping agent. Both can be tuned to control nitrogen defect type and dopant concentration. However, these nitrogen-doping methods simultaneously eliminate oxygen functional groups in GO, which then results in high degrees of aggregation in the prepared *N*-rGO catalysts.[37] This causes most *N*-rGO basal plane surface area to be buried within large aggregates, disallowing any active sites on the basal plane from participating in the ORR catalysis.[16] To this end, a gentle synthesis of *N*-rGO was carefully designed to introduce nitrogen functional groups and minimize oxygen elimination (denoted as *N*-rGO(E)). Briefly *N*-rGO(E) was synthesized through a simple mild thermal treatment with ammonium hydroxide (NH_3OH) as both the nitrogen doping and reduction agent at low temperatures (80 °C). To inhibit aggregation, the as-prepared *N*-rGO(E) was redispersed in ultrapure water from the original reaction solution without drying before the redispersion. A more detailed description is included in the Supporting Information. Incorporation of nitrogen dopants (~5.1 at. %) in *N*-rGO(E) was confirmed using elemental analysis (EA). A second *N*-rGO catalyst (*N*-rGO(H)) was synthesized using a general hydrothermal reaction of GO, urea, and NH_3OH at 140 °C, which created a higher nitrogen content (9.5 at. %) than the mild method mentioned above (a similar redispersion method was also implemented for this material). The total nitrogen and oxygen content in each material studied is shown in Table 1.

Table 1. Atomic Percent of Carbon, Nitrogen, and Oxygen in the Prepared *N*-rGO(E) and *N*-rGO(H) Catalysts Measured by Elemental Analysis

samples	carbon (at. %)	nitrogen (at. %)	oxygen (at. %)
N-rGO(E)	77.8	5.1	17.1
N-rGO(H)	78.8	9.5	11.7

It is worth noting that *N*-rGO materials contain numerous carbon defects associated with oxygen and nitrogen sites, such that a precise chemical structure analysis is unattainable. However, we use here a combination of XPS, NEXAFS, and solid-state NMR to characterize the defect site distributions in each *N*-rGO material as completely as possible. Given the relatively high nitrogen and oxygen concentrations in these materials (Table 1), we expect that both likely consist of small conjugated sp^2 carbon islands that are isolated from each other by regions containing various carbon, oxygen, and nitrogen defects, thereby resulting in low overall material electrical conductivity.[38,39] XPS and NEXAFS results (Figure 1) demonstrate that the two synthetic routes lead to slightly

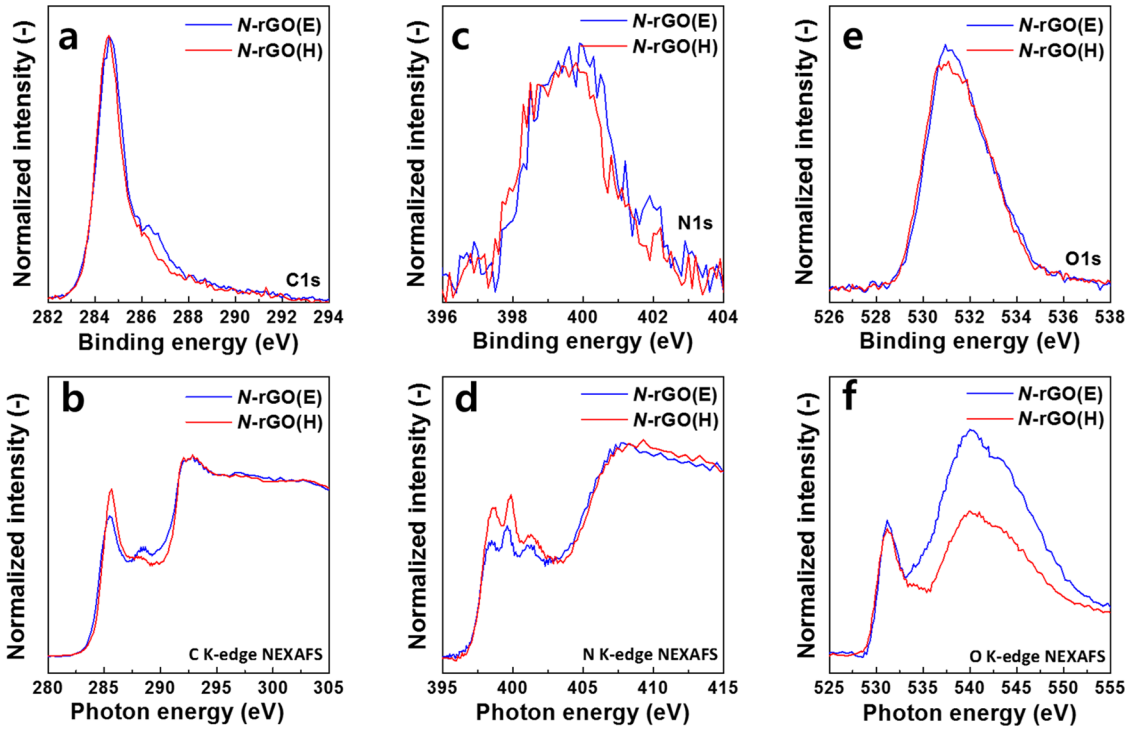

Figure 1. Chemical structures of two *N*-rGO catalysts. (a) High-resolution C 1s, XPS spectra, (b) carbon K-edge NEXAFS spectra, (c) N 1s XPS spectra, (d) nitrogen K-edge NEXAFS spectra, (e) O 1s XPS spectra, and (f) oxygen K-edge NEXAFS spectra of *N*-rGO(E) and *N*-rGO(H) powder samples. All data were collected on powder samples deposited on a Si wafer.

different carbon defects associated with nitrogen and oxygen functionality. For example, a peak present in the *N*-rGO(E) (but not *N*-rGO(H)) C 1s XPS spectra around 287 eV can be ascribed to additional oxygen functional groups on the basal plane in the *N*-rGO(E) (Figure 1a). There are similar differences in the carbon K-edge NEXAFS, namely, that a strong absorption peak at 288 eV that has been previously ascribed to C−O bonding is easily observed in *N*-rGO(E) but is much less pronounced in *N*-rGO(H) (Figure 1b).[40]

In addition, when these C1 XPS spectra (Figure 1a) are compared to that of the starting GO material (Figure S1), the reduction of the peak at 289 eV, which is typically ascribed in the literature to carboxylic acid groups at the edge of GO sheets, indicates that these carboxylic acid functionalities are substantially eliminated during the reduction processes, likely because NH_3OH attacks carboxylic acid groups.[41]

On the other hand, both materials likely contain similar nitrogen defect distributions as analyzed by XPS and NEXAFS (Figure 1c,d), indicating that both *N*-rGOs differ only in total nitrogen content rather than the type of nitrogen defects. Of particular importance, the largest difference between these two materials is their oxygen defect distributions, as is shown by XPS and NEXAFS (Figure 1e,f). This difference is most readily observed in the pronounced difference in the oxygen K-edge NEXAFS starting around 535 eV, where signatures associated with C−O (π^*) and O−H (π^*) are observed, indicating that more epoxy or hydroxyl groups are present in *N*-rGO(E) than in *N*-rGO(H).[16] The oxygen K-edge NEXAFS combined with the C 1s XPS indicate that *N*-rGO(E) possesses more carbon defects related to epoxy and hydroxyl groups than *N*-rGO(H).

To further characterize the defect structure in each material, solid-state ^{13}C NMR coupled with magic angle spinning (^{13}C MAS ssNMR) is performed, with a specific focus on epoxy and hydroxyl groups given the NEXAFS and XPS characterization. The characteristic peaks of these functional groups generally overlap in other commonly used spectroscopic tools, including XPS, which necessitate deconvolution methods that are prone to error. As will be shown here, ^{13}C MAS ssNMR provides a more sensitive analysis of carbon defect composition than XPS or NEXAFS.[42] No studies have correlated ORR activity with defects using ^{13}C MAS ssNMR because the complex structure of GO makes it difficult to attain a high signal-to-noise (S/N) ratio.[43] However, recent advances, including two-dimensional (2D) ^{13}C ssNMR and ^{1}H to ^{13}C cross-polarization CP MAS ($^{1}H-^{13}C$ CPMAS ssNMR), have been implemented to characterize GO's defect structure with great efficacy.[42,43]

The ^{13}C ssNMR analysis indicates that both nitrogen-doping procedures result in a structural change from the pristine starting material, untreated GO (Figure 2). Of note, the direct ^{13}C pulse spectrum of GO is almost identical to literature reports (Figure 2).[42] Also, certain peaks in the GO spectra remain in both *N*-rGO materials. For example, the graphitic sp^2 carbon signal at 120 ppm dominates both *N*-rGO(E) and *N*-rGO(H).[42] This signal is shifted upfield by 9 ppm compared to GO's spectra due to increased electron density of sp^2 carbon, providing evidence of sp^2 carbon restoration in the *N*-rGO samples.[42] A strikingly strong and broad signal in both *N*-rGO powder spectra is observed at around 175 ppm but is not detected in the GO spectra, which is generally assigned to aromatic carboxylic acids or imine (C═N) functionality.[43] However, ammonium hydroxide, which was used as the nitrogen doping and reducing agent in this study, can react with carboxylic acid groups of GO in a similar fashion to an amide hydrolysis reaction.[41] As a result, the peak intensity of the carboxylic acid groups of both materials (289 eV) in C 1s XPS is lower than that of GO (compare Figure 1a and Figure S1).[43] This therefore suggests that the strong signal observed in each material near 175 ppm is due to the presence of a

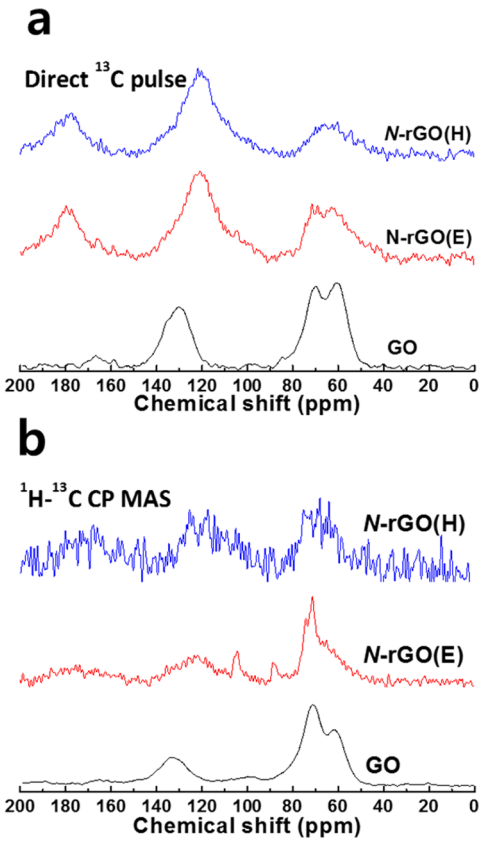

Figure 2. Solid-state ^{13}C MAS NMR spectra of *N*-rGO materials. (a) Direct ^{13}C pulse of *N*-rGO(E), *N*-rGO(H), untreated GO powder samples obtained with 10 kHz MAS, and a 90° ^{13}C pulse (2560 scans). (b) ^{1}H−^{13}C CP spectra of three materials obtained with 10 kHz MAS and a contact time 0.1 ms (1280 scans). The direct ^{13}C MAS experiment can detect all carbon environments, while ^{1}H−^{13}C CPMAS can detect carbons that experience a ^{1}H−^{13}C dipole−dipole interaction, i.e., carbons in covalent proximity to C−H bonds. The direct ^{13}C MAS spectra exhibit three major signals assigned to C−O (60−80 ppm), graphitic C═C (110−130 ppm), and C═N (170−190 ppm) groups.[42−44] On the other hand, the ^{1}H−^{13}C CPMAS reveals signals of carbon associated with specific proton-containing moieties, such as C−OH (70 ppm), C−NH (75 ppm), C−O−CH (88 ppm), and heteroaromatic sp^3 carbon (105 ppm).[42,45,46]

nitrogen-containing functionality, for example, an imine (C═N) as was reported earlier.[44] In particular, a similar intensity between this imine signal and the graphitic sp^2 carbon signals is observed in ^{1}H−^{13}C CPMAS ssNMR (Figure 2b). Considering the low carboxylic acid concentration, as indicated by XPS and NEXAFS analysis, we can ascribe the imine signal centered around 175 ppm to the presence of pyridinic nitrogen groups. In addition, both ^{1}H−^{13}C CPMAS ssNMR spectra, particularly the *N*-rGO(E) spectrum, unveil a new chemical shift at 75 ppm related to pyrrolic nitrogen (C−NH).[45] This signal is difficult to identify by using direct ^{13}C pulse spectra.

Upon comparison of the direct pulse ^{13}C NMR data, a small but visible difference between the *N*-rGO(E) and *N*-rGO(H) samples is the group of peaks in the 40−80 ppm range (Figure 2a). A peak at 60 ppm has been previously ascribed to epoxy groups in GO, whereas a peak near 70 ppm has been ascribed to hydroxyl groups.[42,43] When compared to *N*-rGO(H), *N*-rGO(E) appears to have a slightly stronger signal at both of these chemical shifts, whereas *N*-rGO(H) exhibits a broad peak without separation at those ranges. This implies that *N*-rGO(E) has a slightly higher concentration of epoxy or ether groups on its basal plane than *N*-rGO(H), which is in good agreement with the O K-edge NEXAFS data (Figure 1f).

When comparing the ^{1}H−^{13}C CP-MAS ssNMR spectra of the GO starting material (Figure 2b) and the *N*-rGO(E), we note that all peaks observed in the GO spectrum are also present in the *N*-rGO(E) spectrum, although a few new peaks are observed in the *N*-rGO(E) at 88 and 105 ppm (Figure 2b). This suggests that that mild reduction used to create the *N*-rGO(E) sample allows a reasonable number of carbon defect sites associated with epoxy or ether groups in the GO to remain intact. The peaks at 88 and 105 ppm are consistent with previous reports that ascribed them to protonated carbon next to ether groups and heteroaromatic (especially five-membered ring) carbon, respectively.[42,46] The GO characteristic peaks are much less pronounced, although still present in the *N*-rGO(H) sample.

Taking all above analysis into account, the chemical structures of both *N*-rGO materials can be summarized as follows. First, *N*-rGO(E) and *N*-rGO(H) exhibit almost identical nitrogen defect distributions, but different defect concentrations, with *N*-rGO(H) having a higher nitrogen defect concentration (Table 1). Second, their oxygen defect compositions are dissimilar, with epoxy groups existing at a higher concentration in the *N*-rGO(E) than the *N*-rGO(H). These slight differences should result in different electrochemical ORR activity, which we now discuss for alkaline ORR.

The ORR selectivity and activity of both *N*-rGO catalysts were examined by using methods developed previously.[16] *N*-rGO catalysts were coated on a commercial porous carbon (P50 AvCarb carbon paper) substrate by using a simple dip-coating method.[16] The catalyst loading weight was typically 15 μg/cm^2, similar to the mass loading typically used in electrocatalyst characterization studies.[12,13]

Similar surface areas of both catalysts are obtained from Brunauer−Emmett−Teller (BET) adsorption analysis (Figure S2), indicating that the ORR activity difference between the materials is likely not related to differences in their surface area. The electrodes are characterized in a hermetically sealed H-cell that allows pressure measurements of the calibrated headspace volume to extract precise e^-/O_2 values. O_2-saturated potassium hydroxide (KOH; 0.1 M) dissolved in ultrapure water was used as the electrolyte. The cathodic response of each electrode is examined using linear sweep voltammetry (LSV) at a 2.0 mV/s sweep rate (Figure 3a).

ORR onsets at substantially higher voltages and greater currents are observed at a given overpotential on each *N*-rGO electrode compared to ORR on the uncoated substrate, pristine P50 (Figure 3a). Both catalysts also show superior peroxide activity to high surface area carbon black (Vulcan XC-72, Figure S3). Upon comparison of the two *N*-rGO catalysts to each other, *N*-rGO(E) shows higher activity than *N*-rGO(H) at any given overpotential as well as a higher onset potential. Both catalysts provide excellent selectivity for the $2e^-/O_2$ process, as is observed in Figure 3b,c, which presents oxygen and electron consumption as a function of time at modest overpotentials (0.55−0.70 V_{RHE}) for each catalyst. When performing similar oxygen consumption measurements during LSV, we observe a $2e^-/O_2$ process at all potentials down to 0.1 V_{RHE} (Figure S4). A peroxide titration also indicates that all O_2 consumed at each electrode is converted to peroxide (i.e., a 1.0 O_2/HO_2^- process is observed, Figure

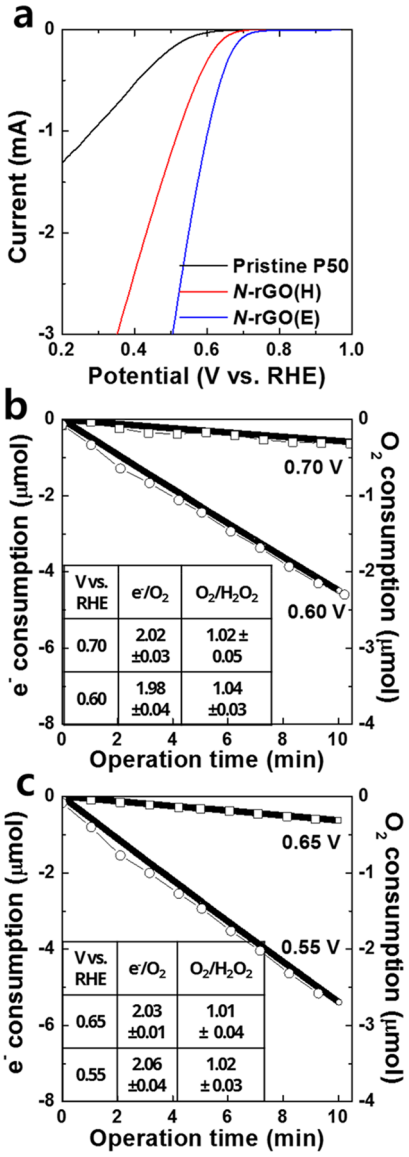

Figure 3. Electrochemical H_2O_2 generation of *N*-rGO(E) and *N*-rGO(H) electrodes. (a) The cathodic LSV of two catalyst-coated electrodes measured at pH 13. The potential sweep rate was 2.0 mV/s, and the initial O_2 pressure was 800 ± 20 Torr. The e^- and O_2 consumption at an *N*-rGO(E) (b) and an *N*-rGO(H) (c) electrode for different applied potentials. Inset table is the ratio of e^-/O_2 from *in situ* measurements and of O_2/H_2O_2, where H_2O_2 formation is measured using an *ex situ* iodometric H_2O_2 titration on the electrolyte after the potentiostatic measurements. These measurements followed a 30 min open circuit potential hold that is not shown.

3b,c).[16] These data taken together indicate that both *N*-rGO catalysts are highly active and selective toward the $2e^-$ ORR reaction, although the *N*-rGO(E) catalyst appears slightly more so given its more anodic onset potential and current rate. Furthermore, the *N*-rGO(E) electrode represents an excellent peroxide forming electrocatalyst at these conditions and is comparable to other high-activity and selectivity electrodes studied in alkaline conditions.[16]

Stable cathodic responses are observed for both materials during ORR at 0.6 V vs RHE for 5 h (Figure S5). Additional ORR activity and kinetic properties are determined from Tafel plots (Figure S6) of both materials acquired using an RDE at 2000 rpm to reduce mass transport limitations in O_2-saturated 0.1 M KOH electrolyte. Assuming Butler–Volmer kinetics govern the ORR mechanism of each catalyst, we extract the Tafel slope, cathodic transfer coefficient, exchange current density, and thermodynamic onset potential using a best fit of the linear region of the Tafel plots (roughly 0.70–0.63 V) (Table 2). Similar Tafel slopes, cathodic transfer coefficients,

Table 2. ORR Activity and Kinetic Parameters

	N-rGO(E)	*N*-rGO(H)
Tafel slope (mV/dec)	86	89
cathodic transfer coefficient	0.30	0.29
exchange current density (A/cm^2)	15×10^{-6}	6.0×10^{-6}
thermodynamic onset potential	0.752 V_{RHE}	0.747 V_{RHE}

and thermodynamic onset potentials are obtained for each material. Among the extracted kinetic parameters, only the exchange current density is substantially different between the two catalysts, with the *N*-rGO(E) exhibiting a roughly 2.5-fold higher exchange current density compared to *N*-rGO(H). This difference likely results from the higher concentration of active sites (related to epoxy, ether groups) in the *N*-rGO(E) material.

To bolster our claim of the importance of epoxy groups over nitrogen-containing groups in the $2e^-$ ORR activity, we have prepared another *N*-rGO material (*N*-rGO(E)-60) following a similar synthetic procedure as the *N*-rGO(E), but with a lower reduction temperature (60 °C rather than 80 °C, as was used for *N*-rGO(E)). The lower reduction temperature resulted in a material with lower nitrogen content compared to *N*-rGO(E) (i.e., 3.2 at. % versus 5.1 at. % for *N*-rGO(E)). The oxygen content of both materials is roughly equivalent, 17.1 at. % for *N*-rGO(E) and 18.5 at. % for *N*-rGO(E)-60 obtained from elemental analysis, as is epoxy content of both materials, as indicated by XPS analysis. However, the *N*-rGO(E)-60 shows comparable peroxide formation activity and identical peroxide selectivity (see Figure S7). This suggests that peroxide production activity is not directly related to the presence of nitrogen functional groups in alkaline electrolytes and is instead related to epoxy groups (as other spectroscopic evidence indicates).

Some interesting conclusions are obtained from these electrochemical data in combination with the chemical structure of the two materials. First, no correlation was observed between nitrogen defect concentrations and onset potentials, as the material with a higher nitrogen-defect concentration had a larger onset overpotential. This also indicates that the carbon defects related to nitrogen functional groups likely have less effect on peroxide formation activity. Instead, based on the structural characterization of the two *N*-rGO materials, our results strongly suggest that oxygen functional groups likely play a pivotal role in HO_2^- generation, which is in strong agreement with our recent study of rGO materials without nitrogen doping, where sp^2 carbon near epoxy or ether groups was identified as the most active site for efficient HO_2^- production in alkaline conditions.[23]

Overall, carbons doped with heteroatoms, especially *N*-rGO, have become increasingly important for oxygen reduction electrocatalysts.[7,19,21,28,29,34,47−49] As a result, many carbon-based electrocatalysts have been developed to promote the ORR; however, material characterization used in most studies only provides limited information about their chemical structure and, hence, possible active sites. In this study, we

have combined XPS, NEXAFS, and direct ^{13}C and $^{1}H-^{13}C$ CP-MAS NMR to elucidate carbon defects related to nitrogen or oxygen defects in *N*-rGO catalysts. Along with electrochemical oxygen reduction results, our data suggest that certain carbon defects associated with epoxy or ether groups have a more pivotal role in promoting peroxide formation activity under alkaline conditions than other functionalities, such as nitrogen defects, quinone/catechol groups, or carboxylic acid edge sites. As a result, this study provides insight into material characterization associated with carbon defects and the electrocatalytic design of carbon-based materials for efficient peroxide generation.

AUTHOR INFORMATION

Corresponding Author

*E-mail: bmcclosk@berkeley.edu.

ORCID

Hyo Won Kim: 0000-0001-7385-796X
Liang Zhang: 0000-0002-3446-3172
Young Hoon Cho: 0000-0002-8863-1979
Vanessa J. Bukas: 0000-0002-0105-863X
Jinghua Guo: 0000-0002-8576-2172
Ho Bum Park: 0000-0002-8003-9698
Tae Hee Han: 0000-0001-5950-7103
Bryan D. McCloskey: 0000-0001-6599-2336

Author Contributions

H.W.K. designed and conducted experiments, and B.D.M. guided experiments. H.W.K. and B.D.M. wrote the manuscript, and all the authors reviewed the manuscript. H.P. synthesized the material, and T.H.H. designed the material synthesis. J.S.R., J.E.S., and T.H.L. characterized the XPS, and H.B.P. helped to analyze the XPS data, L.Z. conducted the NEXAFS, and J.G. provided guideline for the NEXAFS. Y.H.C. and H.W.Y. discussed material characterization. V.J.B had a fruitful discussion concerning the active site. All authors have given approval to the final version of the manuscript.

Notes

The authors declare no competing financial interest.

ACKNOWLEDGMENTS

B.D.M. and H.W.K. gratefully acknowledge support from the National Science Foundation under Grant CBET-1604927. H.W.K. also acknowledges support from the Basic Science Research Program through the National Research Foundation of Korea funded by the Ministry of Education (2016R1A6A3A03012382). T.H.H. and H.P. gratefully acknowledge support from the Basic Science Research Program funded by of the National Research Foundation of Korea (2017R1A2B4010771). H.B.P., J.S.R., J.E.S., and T.H.L. acknowledge support by the Korea CCS R&D Center (Korea CCS 2020 Project) grant funded by the Korea government (Ministry of Science, ICT & Future Planning) in 2018 (Grant 2014M1A8A1049307). This research used resources of the Advanced Light Source, which is a DOE Office of Science User Facility, under Contract DE-AC02-05CH11231.

REFERENCES

(1) Seh, Z. W.; Kibsgaard, J.; Dickens, C. F.; Chorkendorff, I. B.; Norskov, J. K.; Jaramillo, T. F. Combining theory and experiment in electrocatalysis: Insights into materials design. *Science* **2017**, *355* (6321), eaad4998.

(2) Kulkarni, A.; Siahrostami, S.; Patel, A.; Norskov, J. K. Understanding catalytic activity trends in the oxygen reduction reaction. *Chem. Rev.* **2018**, *118* (5), 2302−2312.

(3) Viswanathan, V.; Hansen, H. A.; Rossmeisl, J.; Norskov, J. K. Unifying the $2e^-$ and $4e^-$ reduction of oxygen on metal surfaces. *J. Phys. Chem. Lett.* **2012**, *3* (20), 2948−2951.

(4) Ge, X. M.; Sumboja, A.; Wuu, D.; An, T.; Li, B.; Goh, F. W. T.; Hor, T. S. A.; Zong, Y.; Liu, Z. L. Oxygen reduction in alkaline media: from mechanisms to recent advances of catalysts. *ACS Catal.* **2015**, *5* (8), 4643−4667.

(5) Hansen, H. A.; Viswanathan, V.; Norskov, J. K. Unifying kinetic and thermodynamic analysis of 2 e^- and 4 e^- reduction of oxygen on metal surfaces. *J. Phys. Chem. C* **2014**, *118* (13), 6706−6718.

(6) Jiang, Y.; Ni, P.; Chen, C.; Lu, Y.; Yang, P.; Kong, B.; Fisher, A.; Wang, X. Selective electrochemical H_2O_2 production through two-electron oxygen electrochemistry. *Adv. Energy Mater.* **2018**, *8*, 1801909.

(7) Muthukrishnan, A.; Nabae, Y.; Okajima, T.; Ohsaka, T. Kinetic approach to investigate the mechanistic pathways of oxygen reduction reaction on Fe-containing N-doped carbon catalysts. *ACS Catal.* **2015**, *5* (9), 5194−5202.

(8) Wagman, D. D.; Evans, W. H.; Parker, V. B.; Schumm, R. H.; Halow, I.; Bailey, S. M.; Churney, K. L.; Nuttall, R. L. The NBS tables of chemical thermodynamic properties. *J. Phys. Chem. Ref. Data* **1982**, *11*, 2-37−2-355.

(9) Dai, L.; Xue, Y.; Qu, L.; Choi, H.-J.; Baek, J.-B. Metal-free catalysts for oxygen reduction reaction. *Chem. Rev.* **2015**, *115* (11), 4823−4892.

(10) Hage, R.; Lienke, A. Applications of transition-metal catalysts to textile and wood-pulp bleaching. *Angew. Chem., Int. Ed.* **2006**, *45* (2), 206−222.

(11) Li, J.; Yin, H.-M.; Li, X.-B.; Okunishi, E.; Shen, Y.-L.; He, J.; Tang, Z.-K.; Wang, W.-X.; Yücelen, E.; Li, C.; Gong, Y.; Gu, L.; Miao, S.; Liu, L.-M.; Luo, J.; Ding, Y. Surface evolution of a Pt−Pd−Au electrocatalyst for stable oxygen reduction. *Nat. Energy* **2017**, *2*, 17111.

(12) Siahrostami, S.; Verdaguer-Casadevall, A.; Karamad, M.; Deiana, D.; Malacrida, P.; Wickman, B.; Escudero-Escribano, M.; Paoli, E. A.; Frydendal, R.; Hansen, T. W.; Chorkendorff, I.; Stephens, I. E. L.; Rossmeisl, J. Enabling direct H_2O_2 production through rational electrocatalyst design. *Nat. Mater.* **2013**, *12* (12), 1137−1143.

(13) Verdaguer-Casadevall, A.; Deiana, D.; Karamad, M.; Siahrostami, S.; Malacrida, P.; Hansen, T. W.; Rossmeisl, J.; Chorkendorff, I.; Stephens, I. E. L. Trends in the electrochemical synthesis of H_2O_2: Enhancing activity and selectivity by electrocatalytic site engineering. *Nano Lett.* **2014**, *14* (3), 1603−1608.

(14) Zheng, Z.; Ng, Y. H.; Wang, D. W.; Amal, R. Epitaxial growth of Au-Pt-Ni nanorods for direct high selectivity H_2O_2 production. *Adv. Mater.* **2016**, *28* (45), 9949−9955.

(15) Gong, K. P.; Du, F.; Xia, Z. H.; Durstock, M.; Dai, L. M. Nitrogen-doped carbon nanotube arrays with high electrocatalytic activity for oxygen reduction. *Science* **2009**, *323* (5915), 760−764.

(16) Kim, H. W.; Ross, M. B.; Kornienko, N.; Zhang, L.; Guo, J.; Yang, P.; McCloskey, B. D. Efficient hydrogen peroxide generation using reduced graphene oxide-based oxygen reduction electrocatalysts. *Nat. Catal.* **2018**, *1* (4), 282−290.

(17) Lu, Z.; Chen, G.; Siahrostami, S.; Chen, Z.; Liu, K.; Xie, J.; Liao, L.; Wu, T.; Lin, D.; Liu, Y.; Jaramillo, T. F.; Nørskov, J. K.; Cui,

Y. High-efficiency oxygen reduction to hydrogen peroxide catalysed by oxidized carbon materials. *Nat. Catal.* **2018**, *1* (2), 156−162.
(18) Lin, Z. Y.; Waller, G.; Liu, Y.; Liu, M. L.; Wong, C. P. Facile Synthesis of nitrogen-doped graphene *via* pyrolysis of graphene oxide and urea, and its electrocatalytic activity toward the oxygen-reduction reaction. *Adv. Energy Mater.* **2012**, *2* (7), 884−888.
(19) Qu, L. T.; Liu, Y.; Baek, J. B.; Dai, L. M. Nitrogen-doped graphene as efficient metal-free electrocatalyst for oxygen reduction in fuel cells. *ACS Nano* **2010**, *4* (3), 1321−1326.
(20) Lai, L. F.; Potts, J. R.; Zhan, D.; Wang, L.; Poh, C. K.; Tang, C. H.; Gong, H.; Shen, Z. X.; Lin, J.; Ruoff, R. S. Exploration of the active center structure of nitrogen-doped graphene-based catalysts for oxygen reduction reaction. *Energy Environ. Sci.* **2012**, *5* (7), 7936−7942.
(21) Li, Y. G.; Zhou, W.; Wang, H. L.; Xie, L. M.; Liang, Y. Y.; Wei, F.; Idrobo, J. C.; Pennycook, S. J.; Dai, H. J. An oxygen reduction electrocatalyst based on carbon nanotube-graphene complexes. *Nat. Nanotechnol.* **2012**, *7* (6), 394−400.
(22) Xu, J.; Huang, W. H.; McCreery, R. L. Isotope and surface preparation effects on alkaline dioxygen reduction at carbon electrodes. *J. Electroanal. Chem.* **1996**, *410* (2), 235−242.
(23) Yang, H. H.; McCreery, R. L. Elucidation of the mechanism of dioxygen reduction on metal-free carbon electrodes. *J. Electrochem. Soc.* **2000**, *147* (9), 3420−3428.
(24) Tammeveski, K.; Kontturi, K.; Nichols, R. J.; Potter, R. J.; Schiffrin, D. J. Surface redox catalysis for O_2 reduction on quinone-modified glassy carbon electrodes. *J. Electroanal. Chem.* **2001**, *515* (1−2), 101−112.
(25) Paliteiro, C.; Hamnett, A.; Goodenough, J. B. The electroreduction of oxygen on pyrolytic-graphite. *J. Electroanal. Chem. Interfacial Electrochem.* **1987**, *233* (1−2), 147−159.
(26) Sarapuu, A.; Vaik, K.; Schiffrin, D. J.; Tammeveski, K. Electrochemical reduction of oxygen on anthraquinone-modified glassy carbon electrodes in alkaline solution. *J. Electroanal. Chem.* **2003**, *541*, 23−29.
(27) Rao, C. V.; Cabrera, C. R.; Ishikawa, Y. In search of the active site in nitrogen-doped carbon nanotube electrodes for the oxygen reduction reaction. *J. Phys. Chem. Lett.* **2010**, *1* (18), 2622−2627.
(28) Zitolo, A.; Goellner, V.; Armel, V.; Sougrati, M. T.; Mineva, T.; Stievano, L.; Fonda, E.; Jaouen, F. Identification of catalytic sites for oxygen reduction in iron- and nitrogen-doped graphene materials. *Nat. Mater.* **2015**, *14* (9), 937−942.
(29) Chai, G. L.; Hou, Z. F.; Shu, D. J.; Ikeda, T.; Terakura, K. Active sites and mechanisms for oxygen reduction reaction on nitrogen-doped carbon alloy catalysts: Stone-Wales defect and curvature effect. *J. Am. Chem. Soc.* **2014**, *136* (39), 13629−13640.
(30) Liu, Y.; Quan, X.; Fan, X.; Wang, H.; Chen, S. High-yield electrosynthesis of hydrogen peroxide from oxygen reduction by hierarchically porous carbon. *Angew. Chem.* **2015**, *127* (23), 6941−6945.
(31) Tao, L.; Wang, Q.; Dou, S.; Ma, Z.; Huo, J.; Wang, S.; Dai, L. Edge-rich and dopant-free graphene as a highly efficient metal-free electrocatalyst for the oxygen reduction reaction. *Chem. Commun.* **2016**, *52* (13), 2764−2767.
(32) Zhao, K.; Su, Y.; Quan, X.; Liu, Y.; Chen, S.; Yu, H. Enhanced H_2O_2 production by selective electrochemical reduction of O_2 on fluorine-doped hierarchically porous carbon. *J. Catal.* **2018**, *357*, 118−126.
(33) Iglesias, D.; Giuliani, A.; Melchionna, M.; Marchesan, S.; Criado, A.; Nasi, L.; Bevilacqua, M.; Tavagnacco, C.; Vizza, F.; Prato, M.; Fornasiero, P. N-doped graphitized carbon nanohorns as a forefront electrocatalyst in highly selective O_2 reduction to H_2O_2. *Chem.* **2018**, *4* (1), 106−123.
(34) Guo, D. H.; Shibuya, R.; Akiba, C.; Saji, S.; Kondo, T.; Nakamura, J. Active sites of nitrogen-doped carbon materials for oxygen reduction reaction clarified using model catalysts. *Science* **2016**, *351* (6271), 361−365.
(35) Bowling, R. J.; Packard, R. T.; Mccreery, R. L. Activation of highly ordered pyrolytic-graphite for heterogeneous electron-transfer - relationship between electrochemical performance and carbon microstructure. *J. Am. Chem. Soc.* **1989**, *111* (4), 1217−1223.
(36) Shen, A. L.; Zou, Y. Q.; Wang, Q.; Dryfe, R. A. W.; Huang, X. B.; Dou, S.; Dai, L. M.; Wang, S. Y. Oxygen reduction reaction in a droplet on graphite: Direct evidence that the edge is more active than the basal plane. *Angew. Chem., Int. Ed.* **2014**, *53* (40), 10804−10808.
(37) Cote, L. J.; Kim, F.; Huang, J. X. Langmuir-Blodgett assembly of graphite oxide single layers. *J. Am. Chem. Soc.* **2009**, *131* (3), 1043−1049.
(38) Bukas, V. J.; Kim, H. W.; Sengpiel, R.; Knudsen, K. B.; Voss, J.; McCloskey, B. D.; Luntz, A. C. Combining experiment and theory to unravel the mechanism of two-electron oxygen reduction at a selective and active co-catalyst. *ACS Catal.* **2018**, *8* (12), 11940−11951.
(39) Eda, G.; Chhowalla, M. Chemically derived graphene oxide: towards large-area thin-film electronics and optoelectronics. *Adv. Mater.* **2010**, *22* (22), 2392−2415.
(40) Ji, L.; Rao, M.; Zheng, H.; Zhang, L.; Li, Y.; Duan, W.; Guo, J.; Cairns, E. J.; Zhang, Y. Graphene oxide as a sulfur immobilizer in high performance lithium/sulfur cells. *J. Am. Chem. Soc.* **2011**, *133* (46), 18522−18525.
(41) Dreyer, D. R.; Park, S.; Bielawski, C. W.; Ruoff, R. S. The chemistry of graphene oxide. *Chem. Soc. Rev.* **2010**, *39* (1), 228−240.
(42) Gao, W.; Alemany, L. B.; Ci, L. J.; Ajayan, P. M. New insights into the structure and reduction of graphite oxide. *Nat. Chem.* **2009**, *1* (5), 403−408.
(43) Cai, W. W.; Piner, R. D.; Stadermann, F. J.; Park, S.; Shaibat, M. A.; Ishii, Y.; Yang, D. X.; Velamakanni, A.; An, S. J.; Stoller, M.; An, J. H.; Chen, D. M.; Ruoff, R. S. Synthesis and solid-state NMR structural characterization of ^{13}C-labeled graphite oxide. *Science* **2008**, *321* (5897), 1815−1817.
(44) Khandelwal, M.; Kumar, A. One-pot environmentally friendly amino acid mediated synthesis of N-doped graphene-silver nanocomposites with an enhanced multifunctional behavior. *Dalton Trans.* **2016**, *45* (12), 5180−5195.
(45) Xiao, P. W.; Guo, D.; Zhao, L.; Han, B. H. Soft templating synthesis of nitrogen-doped porous hydrothermal carbons and their applications in carbon dioxide and hydrogen adsorption. *Microporous Mesoporous Mater.* **2016**, *220*, 129−135.
(46) Park, S.; Baker, J. O.; Himmel, M. E.; Parilla, P. A.; Johnson, D. K. Cellulose crystallinity index: measurement techniques and their impact on interpreting cellulase performance. *Biotechnol. Biofuels* **2010**, *3* (1), 10.
(47) Wu, G.; More, K. L.; Johnston, C. M.; Zelenay, P. High-performance electrocatalysts for oxygen reduction derived from polyaniline, iron, and cobalt. *Science* **2011**, *332* (6028), 443−447.
(48) Liang, Y. Y.; Li, Y. G.; Wang, H. L.; Zhou, J. G.; Wang, J.; Regier, T.; Dai, H. J. Co_3O_4 nanocrystals on graphene as a synergistic catalyst for oxygen reduction reaction. *Nat. Mater.* **2011**, *10* (10), 780−786.
(49) Zhang, J. T.; Zhao, Z. H.; Xia, Z. H.; Dai, L. M. A metal-free bifunctional electrocatalyst for oxygen reduction and oxygen evolution reactions. *Nat. Nanotechnol.* **2015**, *10* (5), 444−452.